

From schwertmannite to natrojarosite: Long-term stability and kinetic approach

AMALIA JIMÉNEZ^{1,*}, GREGORIO MARBAN², AND ANA ROZA-LLERA¹

¹Departamento Geología, Universidad de Oviedo, 33005-Oviedo, Spain

²Instituto Nacional del Carbono, CSIC, Francisco Pintado Fe, 26, 33011-Oviedo, Spain

ABSTRACT

This work examines the transformation of iron-bearing precursors to jarosite-like minerals in the absence of bacteria or other organic compounds. The composition of the aqueous solution determines the transformation, through which crystallinity and long-term stability of jarosite increase, whereas the temperature of the environment affects the kinetics of the process. Spectroscopic techniques (FTIR and XPS) were used to characterize the chemical species present on the transformed mineral surfaces. Schwertmannite is the first phase to precipitate as a result of homogeneous nucleation and growth in the bulk of the supersaturated solution. This metastable phase transforms into a crystalline Na-rich member of the $(\text{Na},\text{H}_3\text{O})\text{Fe}_3(\text{SO}_4)(\text{OH})_6$ solid-solution family after aging for either 3 h at 70 °C or 1 day at 20 °C. XRD analyses show that the crystallinity of natrojarosite increases progressively with reaction time, although its cell parameters and crystallite size remain nearly constant during aging, which reveals the stability of the crystal structure of this secondary phase. Interestingly, the mechanisms governing the transformation from aggregates of schwertmannite into natrojarosite crystals consist of interface-coupled dissolution–precipitation reactions that involve an internal structural reorganization within the individual nanoparticles of the secondary phase, in which Fe^{3+} is transferred from the solid to the solution while SO_4^{2-} , OH^- , and Na^+ move in the opposite direction. The spectroscopic study confirms the mineralogical results and suggests that the crystal structure of jarosite-like minerals may offer interesting geochemical information about the aqueous solutions where they were formed. The transformation kinetics and the apparent activation energy ($E_a = 52.1$ kJ/mol) of the transformation were estimated using the so-called “time to a given fraction” method, and a temperature–transformation-time (TTT) diagram was established in the range 20–70 °C to define the reaction pathways during the process.

Keywords: Schwertmannite, natrojarosite, precipitation, stability, kinetic, spectroscopy, acidic conditions


INTRODUCTION

The precipitation of iron-bearing metastable phases is a common process in natural and anthropic environments, where they precipitate whenever water is present under acidic conditions (Schwertmann et al. 1995; Bigham et al. 1996; Bigham and Nordstrom 2000; Gagliano et al. 2004). Schwertmannite (Shm), a poorly crystalline Fe(III)-oxyhydroxysulfate of ambiguous composition, has attracted the interest of researchers because sulfate can be substituted by a range of oxyanions (AsO_4^{3-} , CrO_4^{2-} , SeO_4^{2-} , PO_4^{3-}). Moreover, its unique physicochemical properties, such as high surface area (125–320 m²/g) (Bigham et al. 1990), explain its high reactivity and capacity to retain toxic ions via adsorption and coprecipitation processes (Waychunas et al. 1995; Acero et al. 2006; Sánchez-España et al. 2006; Asta et al. 2009; Burton et al. 2009). It is well-known that precipitation of schwertmannite is followed by transformation into more crystalline and stable phases such as jarosites [$M\text{Fe}_3(\text{SO}_4)_2(\text{OH})_6$, where $M = \text{Na}^+$, H_3O^+ , K^+ , Ag^+ , NH_4^+ , or $1/2\text{Pb}_2^+$], goethite (αFeOOH) and

hematite (Fe_2O_3). These latter phases control the solubility of iron-bearing minerals over a wide pH range (Waychunas et al. 1995; Bigham et al. 1996; Barham 1997; Gagliano et al. 2004; Jönsson et al. 2005; Desborough et al. 2010; Sánchez-España et al. 2012). For this reason, although some studies claim the efficiency of Shm to sequester heavy metals (Acero et al. 2006; Burton et al. 2009), others reveal that pollutants are released to the aqueous solution during mineral transformation on a short timescale (Regenspurg and Peiffer 2005; Sánchez-España et al. 2006; Cruz-Hernández et al. 2016).

Understanding the schwertmannite transformation into jarosite-like minerals has a special interest in geological, environmental, and planetary science. For instance, secondary jarosite minerals are associated with supergene minerals in ore deposits, acid sulfate soils, acid-mine drainage, and hydrometallurgical processes involving oxidation of iron sulfide minerals (Bigham and Nordstrom 2000). The formation of jarosite during early weathering processes and its presence in epithermal deposits, which are formed at low-hydrothermal temperatures (from 50 to 200 °C) and shallow depths (Arribas 1995), explain the importance of these minerals for prospecting and mining. The low solubility of jarosite-like minerals,

* E-mail: amjimenez@uniovi.es

 Open access: Article available to all readers online. This article is CC-BY-NC-ND.

together with the flexibility of its crystalline structure, which allows the incorporation of different foreign ions such as rare earths or toxic metals, determines their geochemical and environmental significance (Dutrizac 1996; Acero et al. 2006; Asta et al. 2009). The precipitation of jarosite requires dry conditions after mineral precipitation (Nordstrom 2009), typical of the transition from humid or semi-arid to hyperarid conditions that occurred in the past on Mars' surface (Fairén et al. 2010). Thus, the identification of jarosite on Mars has been interpreted as an indicator of arid climate and water-limited chemical weathering (Burns 1987; Madden et al. 2004).

Although numerous studies have been conducted on both the sorption capacity of Fe(III) hydroxysulfate and the fate of the toxic ions during transformation, relatively few works have examined the precipitation behavior and subsequent transformation from the precursor to the crystalline phase under highly acidic condition ($\text{pH} < 3$) and low hydrothermal temperatures. However, the precipitation of metastable phases is strongly influenced by kinetic and other physicochemical parameters, such as pH, that modify the distribution of chemical species in the aqueous phase, which in turn, facilitates the transformation of these phases into more stable phases (Jiménez et al. 2019). In this context, the effect of changes in the geochemical conditions (aqueous and solid-phase compositions, temperature, and pH) on the long-term stability of jarosite in acidic aqueous systems deserves further study. Spectroscopic techniques (FTIR and XPS) have allowed various minerals of the jarosite group to be identified (Dutrizac and Kaiman 1976; Gagliano et al. 2004; Bishop and Murad 2005; Basciano and Peterson 2007, 2008; Majzlan et al. 2011), but they can also be used to shed light on the geochemical conditions of the medium where minerals are formed.

This work aims to study the crystallization behavior of natrojarosite by direct precipitation from supersaturated solutions at both ambient (20 °C) and low (70 °C) hydrothermal temperatures. Specific experiments have been designed to attain a rapid transformation from poorly crystalline (schwertmannite) to crystalline phases (natrojarosite), in which precipitation occurs after shorter periods of time than those needed in our previous study performed with parent solutions of low and intermediate concentrations at ambient temperature (Jiménez et al. 2019). X-ray diffraction and scanning electron microscopy were used to follow the mineral transformation and the long-term stability of the crystalline phases. Fourier-transform infrared spectroscopy and X-ray photoelectron spectroscopy techniques in combination with X-ray diffraction were used to characterize the chemical species at the natrojarosite surface. The kinetics and the activation energy of the transformation of schwertmannite into natrojarosite are analyzed using the so-called "time to a given fraction" method (Putnis 1992), and a temperature-transformation-time (TTT) diagram was constructed to define the reaction pathways during the process. The highly acidic and sulfate-rich solutions used in

this work are analogous to those of acid mine drainages and to the ancient waters of Mars (Nordstrom 2009; Fairén et al. 2010).

METHODS

Synthesis of iron hydrosulfates

Two sets of precipitates were produced by aging two different aqueous solutions of $\text{Fe}_2(\text{SO}_4)_3$ and NaOH (0.12 and 0.2 M for the LC20 samples and 0.20 and 0.4 M for the HC20 samples) at ambient temperature (~ 20 °C) for various durations from 3 h to 210 days. The pH and composition of the initial aqueous solutions are given in Table 1. The composition of the parent solutions was selected to obtain stable phases faster than in our previous study (Jiménez et al. 2019). Additionally, the effect of temperature on the nature of the precipitates was checked by introducing the starting solutions (Table 1) in a thermostatic reactor preheated at 70 °C (LC70 and HC70 samples for the low and high concentrated solutions, respectively) for 3 h. After preparing the solutions, all the reaction vessels were sealed to avoid evaporation and maintained under constant stirring (100 rpm). All precipitates were produced in triplicate using deionized (MilliQ) water and analytical grade reagents.

The solution pH was measured at the beginning and the end of the aging process with a combination electrode (Ross-Thermo-Orion-810200) and a digital pH meter (Crison Basic20). The solid and liquid phases were separated by centrifugation for 10 min at 3000 rpm in a Rotina 380. The initial aqueous solutions were modeled using the geochemical code PHREEQC (Parkhurst and Appelo 1999) and the WATEQ4F database to calculate the activities of different chemical species and saturation indexes (SI) with respect to the relevant solid phases at the beginning of the experiments. The database was completed with the thermodynamic solubility product of Shm ($K_{sp} = 10^{-5.28}$) (Yu et al. 1999).

Characterization of solid phases

The precipitates were oven-dried at 30 °C and then gently crushed to a fine powder using an agate mortar and analyzed by powder X-ray diffraction (XRD). The diffraction patterns were collected in the 2θ range between 5° and 60° with a step size of 0.02° on a Philips X'Pert-PRO diffractometer using $\text{CuK}\alpha$ radiation. Indexing of the main reflections and calculation of the cell parameters of the solid phases were made using X'Pert HighScore Plus (PANalytical B.V.). The crystallinity of the samples was determined from the full-width at half maximum values (FWHM) of the highest d -spacing and more intense reflections. The FWHM values were established after performing a $K\alpha 2$ stripping and then applying the Pseudo-Voigt profile fitting function. Moreover, the crystallite size of samples was roughly estimated using the X'Pert Plus "Scherrer calculator" tool. Morphology of solids was studied using a scanning electron microscopy (SEM) (JEOL-6610). Transmission Fourier transform infrared spectroscopy (FTIR) spectra of the powdered samples compressed into discs with KBr were recorded from 400 to 4000 cm^{-1} on a Nicolet Magna IR 560 spectrometer fitted with a DTGS absorbance detector.

The surface of the precipitates was analyzed by ex-situ X-ray photoelectron spectroscopy (XPS) with a Specs spectrometer, using $\text{MgK}\alpha$ or $\text{AlK}\alpha$ (30 eV) radiation emitted from a double anode at 50 W. The binding energies of the resulting spectra were corrected by employing the binding energy of adventitious carbon (284.6 eV) in the C1s region or the binding energy of Na^+ (1071.7 eV) in the Na1s region. The backgrounds were corrected using Shirley's baselines. All the analyzed regions (C1s, O1s, Na1s, Fe2p $_{3/2}$, and S2p) were deconvolved by means of mixed Gaussian-Lorentzian functions (90:10). The quantitative analyses were based on atomic sensitivity factors stored in the CasaXPS database (v2.3.12Dev6).

Isothermal experiments

The transformation of the metastable phase (schwertmannite, Shm) to the stable ones (natrojarosite, NaJrs) was studied for the precipitates obtained from the highest concentrated starting solutions (HC experiments). The procedure begins by mixing the starting solutions at ambient conditions (20 ± 1 °C) and then putting them in a thermostatic bath to predetermined temperatures (20, 35, 50, or 70 °C), where the mixture was maintained at isothermal conditions during reaction times varying between 0.5 and 26 h. The transformation extent of Shm into NaJrs with increasing time has been checked by examining the most important reflections of NaJrs (012, 021, and 113) by using X'Pert Viewer. We considered this scenario to establish an extent of transformation up to about 95% ($Y \sim 95\%$). A more precise quantification of crystalline vs. poorly crystalline phases to assess the transformation extent requires a Rietveld analysis, which is out of the scope of the present work.

TABLE 1. Initial pH and concentration of iron [Fe], sodium [Na], and sulfate [SO_4] used in the experiments performed by mixing parent solutions with low concentration (LC) and high concentration (HC)

Experiments	pH	[Fe] g/L	[Na] g/L	[SO_4] g/L
LC	2.41 \pm 0.2	13.40 \pm 0.09	4.60 \pm 0.11	11.54 \pm 0.11
HC	2.59 \pm 0.3	22.12 \pm 0.12	9.16 \pm 0.10	19.04 \pm 0.12

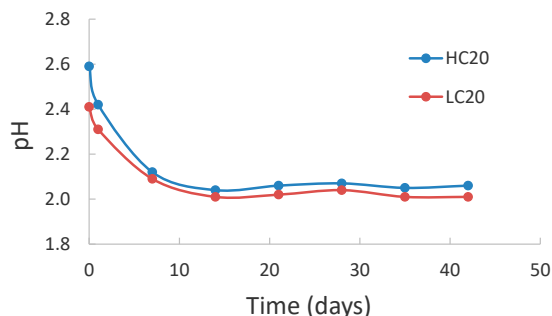


FIGURE 1. Variation of pH with time during aging at 20 °C. (Color online.)

RESULTS

Evolution of the aqueous pH during precipitation at ambient temperature

Figure 1 shows the evolution of the pH of the aqueous solution as a function of time for the experiments carried out at 20 °C (LC20 and HC20). As can be observed, the pH quickly decreases during the first day of aging and approaches asymptotic values of about 1.89 after 42 days. The variation of pH values is negligible or within the experimental uncertainties in solutions maintained for prolonged reaction times (210 days).

XRD analysis

The X-ray powder diffraction patterns of the LC precipitates are shown in Figure 2. The diffractogram of the precipitate obtained after 1 day of reaction at 20 °C shows two humps at 2θ of $\sim 35^\circ$ and $\sim 61^\circ$ that match the schwertmannite pattern (PDF-47-1775). Schwertmannite is a poorly crystalline phase, which was recognized as a mineral regardless of its metastability (Bigham et al. 1994; Barham 1997; Acero et al. 2006). The general formula

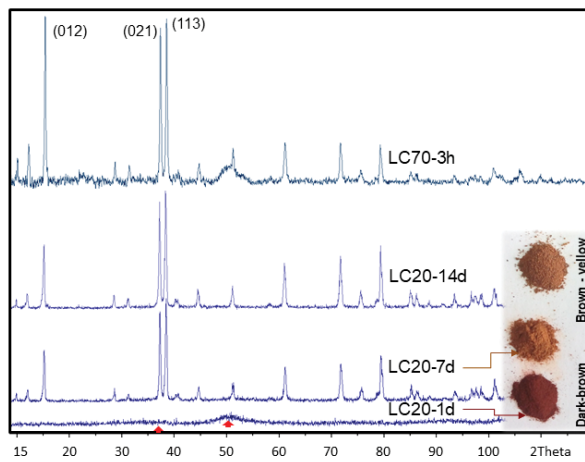


FIGURE 2. X-ray diffractograms of the solid phases obtained during aging LC experiments. Broad diffraction peaks of schwertmannite (PDF 47-1775) are marked with arrows. The main diffraction peaks of natrojarosite (PDF 36-425) are identified after prolonged times at 20 °C and after 3 h of aging at 70 °C. The evolution of color of the precipitates obtained in experiments at ambient temperature are also included. (Color online.)

of schwertmannite is $\text{Fe}_8\text{O}_8(\text{OH})_{8-2x}(\text{SO}_4)_x \cdot n\text{H}_2\text{O}$ (with x varying from 1 to 1.9). Although the first studies proposed that Shm crystallizes in the tetragonal system (Bigham et al. 1994) with a space group $P4/m$, a monoclinic structure (space group $P1$) was finally resolved by combining high-energy X-ray diffraction and theoretical simulations in which the position of water molecules was disregarded (Fernandez-Martinez et al. 2010). It must be mentioned that 2-line ferrihydrite [$\text{Fe}_{10}\text{O}_{14}(\text{OH})$] produces a similar XRD pattern to that of Shm, but it precipitates at neutral pH at ambient temperature (Bigham et al. 1996; Yu et al. 1999), whereas Shm always precipitates under highly acidic conditions ($\text{pH} < 4$ values), which are the prevalent conditions in this work (Fig. 1). The precipitates obtained after aging at 20 °C (LC20-7d and LC20-14d) and 70 °C (LC70-3h) display the typical reflections of natrojarosite (PDF 36-425) [$\text{NaFe}_3(\text{SO}_4)_2(\text{OH})_6$], which crystallizes in the trigonal system ($R3m$ space group 160). Other crystalline phases such as hematite or goethite were not identified in the samples aged up to 42 days at 20 °C. In parallel to the evolution of phases, the color of the precipitates obtained at 20 °C changes from brown-reddish in the first moments to brown-yellow at the end of reaction (Fig. 2).

The diffraction patterns of the HC20 precipitates (Fig. 3) reveal that schwertmannite precipitates at the beginning of the experiments (HC20-3h). However, incipient reflections at 2θ of $\sim 17.61^\circ$, $\sim 28.65^\circ$, and $\sim 29.29^\circ$ observed in the diffraction patterns obtained after 1 day of aging (HC20-1d) indicate the existence of a phase with some degree of crystallinity that becomes more apparent with further aging (Fig. 3). These reflections match the main XRD reflections (012, 021, and 113) of natrojarosite [$\text{NaFe}_3(\text{SO}_4)_2(\text{OH})_6$]. No further advance in the mineral transformation is observed after long-period reactions (210 days). Furthermore, the transformation from a poorly crystalline phase to natrojarosite is also evidenced by the change of color of the precipitates for increasing aging times, from dark brown to yellow-brown (Fig. 3). The diffraction patterns obtained for the precipitates produced at 70 °C (Fig. 3) clearly match that of the natrojarosite.

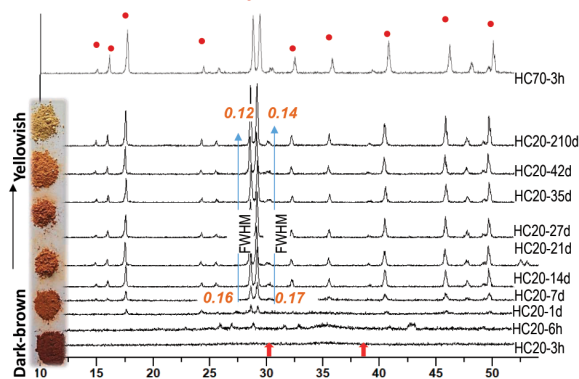


FIGURE 3. X-ray diffraction patterns of the solid obtained during aging HC experiments. Diffraction peaks for poorly crystalline phase are marked with arrows. The main reflections of natrojarosite (PDF 36-425) are signaled with gray points. The evolution of color of precipitates from the beginning to the end of the experiments is included. The increase of crystallinity of natrojarosite during aging is indicated by italic numbers of the FWHM values (2θ) of reflections 021 and 113. (Color online.)

The unit-cell parameters of natrojarosite calculated from the powder diffraction diagrams show similar values for all the HC20 precipitates ($a \sim 7.325 \pm 0.010 \text{ \AA}$ and $c \sim 16.842 \pm 0.080 \text{ \AA}$), regardless of the increase of crystallinity. The unit-cell parameters of the sodium-hydronium jarosite series decrease with increasing Na content because of the lower size of Na^+ ions in comparison with H_3O^+ ions (Basciano and Peterson 2008). Jarosite-type compounds often have iron deficiency, with Fe-site occupancies lower than 86%, which seems to be responsible for discrepancies in the unit-cell parameters (Brophy and Sheridan 1965; Drouet and Navrotsky 2003; Basciano and Peterson 2007). A good estimation of the composition of the precipitates can be obtained from the position of reflection 006, being 32.19 (2θ) for pure natrojarosites, whereas it takes a value of 31.53 for pure hydronium-jarosite. For intermediate compositions, the 006 reflection could broaden or split up into two peaks, the latter indicating the presence of a miscibility gap. Here, the position of the 006 reflections (~ 32.17 , 2θ) is near that of the pure natrojarosite, with no broadening or splitting of this reflection observed in the diffractograms (Fig. 3). Thus, from the unit-cell dimensions and the 006 reflection, HC20 and HC70 precipitates can be identified as Na-rich members of the $(\text{Na}, \text{H}_3\text{O})\text{Fe}_3(\text{SO}_4)(\text{OH})_6$ solid solution (NaJrs).

The crystallinity of the HC20 precipitates was also examined from the broadening (FWHM) of the most intense reflections 021 and 113 of NaJrs. The decrease of FWHM values of both reflections, along with the increase of their intensity observed from XRD (Fig. 3), confirm the increase of crystallinity during aging (Langford and Wilson 1978). Working with the FWHM of the 113 reflections, i.e., the reflections with the highest intensity, the crystallite size can be estimated to be 66 nm for NaJrs. As it is widely known, the crystallite size represents the size of the coherently diffracting domain and not the size of the precipitate particles.

SEM

The electron images of the precipitates obtained at different temperatures (20 and $70 \text{ }^\circ\text{C}$) are shown in Figure 4. SEM images of schwertmannite obtained in the LC20 precipitates show that their surface is constituted by an agglomerate of nanospheres (Fig. 4a), formed from the fast precipitation of discrete colloidal particles that prevent the incorporation of growth units to the mineral surface (Sangwal 1999). After 14 days of aging, the agglomerate evolves to crystals of natrojarosite displaying an

equidimensional habit ($\sim 1 \text{ }\mu\text{m}$ size) whose morphology could be similar to pseudo-rhombohedral (Fig. 4b). Similarly, the evolution of the crystallinity with aging is observed in the HC20 precipitates. SEM images show that aggregates of small crystals with shapeless morphology at the beginning of the aging process gain the typical rhombohedral morphology of natrojarosite, showing well-defined faces and edges after 42 days of aging (Fig. 4c).

FTIR

Figure 5 shows the FTIR spectra obtained for HC70-3h and LC70-3h samples. The peaks at $970\text{--}995 \text{ cm}^{-1}$ (LC70) and 991 cm^{-1} (HC70) are assigned to the symmetric ν_1 stretching of SO_4^{2-} , whereas the bands at $1088/1093 \text{ cm}^{-1}$ and the shoulders at $1185/1190 \text{ cm}^{-1}$ (HC70/LC70) are attributed to the ν_3 (doublet) vibrations of SO_4^{2-} (Powers et al. 1975; Majzlan et al. 2011; Sotiropoulou et al. 2012). The shoulder at 1025 cm^{-1} may be attributed both to the ν_1 vibration of sulfate and to the Fe-O-H in-plane-bend (δOH) (Powers et al. 1975; Majzlan et al. 2011; Sotiropoulou et al. 2012). The adsorption band at around 613 cm^{-1} is assigned to the asymmetric ν_4 bending motion of sulfate (Bishop and Murad 2005). The wide band centered at $3310\text{--}3345 \text{ cm}^{-1}$ is characteristic of the ν stretching of O-H (Casas et al. 2007). All these bands are characteristic of natrojarosite. However, some other features in the spectra of Figure 5 must originate from a different source. For instance, the conspicuous band at 1635 cm^{-1} corresponds to the water-bending vibration (Bishop and Murad 2005; Majzlan et al. 2011), but it is present in synthetic jarosite samples where H_3O^+ replaces some of the monovalent sites (Grohol and Nocera 2002; Majzlan et al. 2011). This band is usually weak in natrojarosite and jarosite (Powers et al. 1975; Majzlan et al. 2011; Sotiropoulou et al. 2012). The peak at 795 cm^{-1} is also absent in natrojarosite (Casas et al. 2007). On the other hand, its frequency is characteristic of the out-of-plane deformational (γ) mode of hydroxyls in goethite (Prasad et al. 2006). The band at 1635 cm^{-1} can also be attributed to a bending mode of hydroxyls in goethite, though in natural goethite it is significantly weaker than the peak at 795 cm^{-1} (Prasad et al. 2006), and therefore the assignation of the 1635 cm^{-1} frequency to H_3O^+ prevails. The presence of a small fraction of goethite is further confirmed by the shoulder at around 3130 cm^{-1} , which corresponds to the stretching mode of hydroxyls in FeOOH (Prasad et al. 2006). Finally, two main features can be found in the $400\text{--}500 \text{ cm}^{-1}$ region ($460\text{--}465$ and $490\text{--}495 \text{ cm}^{-1}$). Both of

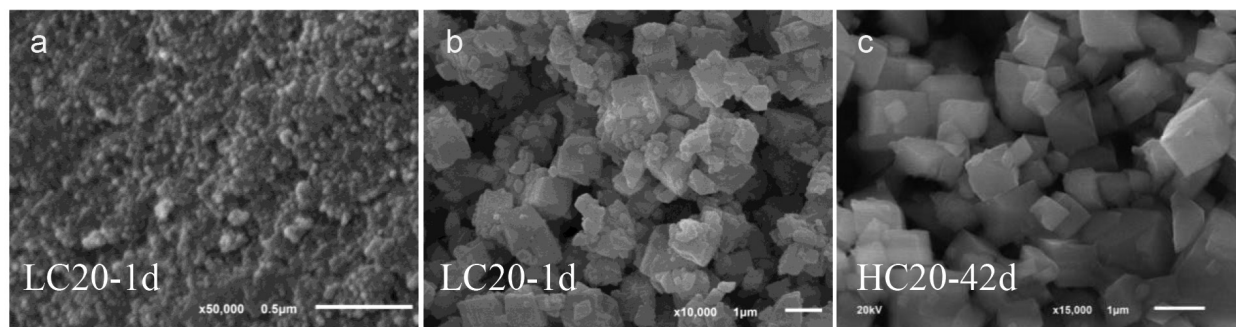


FIGURE 4. SEM images of iron hydroxysulfates. (a) The surface of schwertmannite is composed by aggregate of particles. (b) Natrojarosite crystals. (c) Rhombohedral crystals of natrojarosite.

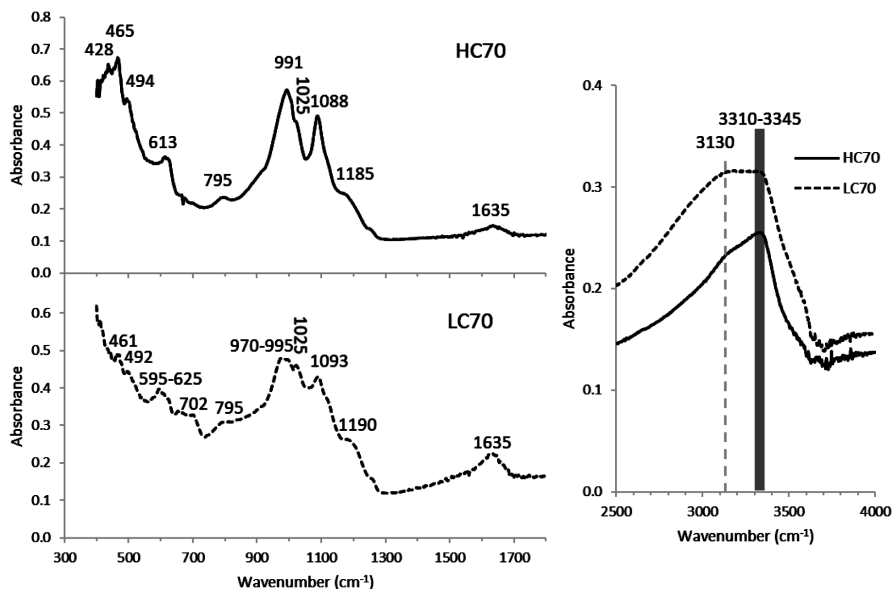


FIGURE 5. FTIR spectra for precipitates obtained for HC70-3h and LC70-3h.

them are attributed to vibration modes of the FeO_6 lattice. The low-wavenumber mode can originate from goethite (Prasad et al. 2006), hydronium jarosite (Powers et al. 1975), and goethite-natrojarosite mixtures (Casas et al. 2007), whereas the $\sim 495 \text{ cm}^{-1}$ frequency can be attributed to natrojarosite (Casas et al. 2007) and hydronium jarosite (Powers et al. 1975). Added to this, a small fraction of the surface iron remains as goethite. The XPS results will help in the quantification of these surface species.

XPS

The elemental composition of the different samples obtained from the XPS analyses is shown in Table 2. In all cases, the amount of surface iron is much lower than that corresponding to natrojarosite (15 at%), but the proportion of the remaining elements is more similar to that of this mineral (70% O, 10% S and 5% Na). The amount of iron evaluated with the $\text{AlK}\alpha$ source is always higher than that evaluated with the $\text{MgK}\alpha$ source. Since the latter produces photoelectrons from a slightly thinner layer of the sample surface, it can be concluded that the iron concentration increases toward the center of the particles, probably to the limit of 15 at% marked by the natrojarosite stoichiometry (in accordance with the XRD results). This fact suggests that the bulk sodium concentration for all the samples is again that corresponding to natrojarosite (5 atoms%). On the other hand, when the surface concentration of sodium is over 5 at% (HC samples) it decreases toward the center of the particles (Table 2), but when the sodium concentration is below 5 at% (LC samples), it increases toward the center of the particles.

TABLE 2. XPS surface composition (atom%) for the different samples

Sample	O	S	Fe	Na
HC70 (MgK α)	74.68	11.85	6.32	7.15
HC70 (AlK α)	75.28	10.82	6.95	6.95
LC70 (MgK α)	76.72	14.85	4.82	3.62
LC70 (AlK α)	76.31	13.31	5.63	4.74
LC20 (MgK α)	73.92	20.77	4.32	1.00

With respect to the determination of the different surface compounds, XPS is an analytical tool that has to be used cautiously, and the present analysis is a perfect example of this assessment. Online Materials¹ Figure S1 shows a region subjected to deconvolution in two different ways (top and bottom), in which only a deconvolution procedure similar to that presented in the top plot permits us to satisfy the charge balance for all the samples without the need of including unlikely species (see the Online Material¹ for further explanation).

Figure 6 shows the results of applying the appropriate deconvolution procedure to all spectra in the O1s region, whose binding energies were corrected by employing the binding energy of

adventitious carbon (284.6 eV). The vertical lines indicate the average values (530.1 ± 0.1 , 531.4 ± 0.1 , and 532.0 ± 0.2 eV) for the three peaks needed in the deconvolutions. The O1s spectra obtained with the $\text{AlK}\alpha$ source (right plots in Fig. 6) were affected by the Na KLL region in the form of a wide peak at 535.8 eV. The small peak at 530.1 eV is assigned to O^- in FeOOH (Jin et al. 2020), whereas the peak at 531.4 eV includes the contribution of oxygen atoms in the sulfate anion (Gard et al. 2020) and hydroxyls (Grosvenor et al. 2004; Liu et al. 2014; Khalid et al. 2017; Gard et al. 2020). Finally, the peak at 532.0 eV is assigned here to hydronium ions (H_3O^+), consistent with the FTIR results. This peak might be well enclosed within the hydronium jarosite standard spectrum reported by Parker (2008) (Fig. 6). Furthermore, assignation of this peak to adsorbed water molecules, as is often the case (Diao et al. 2018; Cheng et al. 2020) would make it impossible for charge balance to be satisfied. As can be observed in Figure 6, the maxima of the different peaks present some deviation with respect to the average values (dashed lines). These spectra were taken by assuming that the binding energy for the maximum of the C1s region (284.6 eV) was a valid reference. However, during the XPS analyses, the samples suffer intense surface charging, evidenced by a high-binding energy shift of 2.8 ± 0.2 eV, meaning that the samples are non-conducting. Within this frame, the referencing method involving adventitious carbon in the C1s region is not reliable (Greczynski and Hultman 2020). The XPS regions produced by Na^+ and sulfur from SO_4^{2-} display single-peak spectra (Fig. 7) whose characteristic binding energies should be, in principle, independent of the type of sample. Therefore, we decided to change the C1s referencing method and use the binding energy of Na1s instead, averaged for all samples. This is, in fact, the standard binding energy for sodium ions (Na^+) (Feliu et al. 2013). As can be observed in Table 3, with the new referencing method, the standard deviation values for the maxima of O1s and S2p peaks are reduced. As expected, the peak at 168.9 eV corresponds to sulfur from

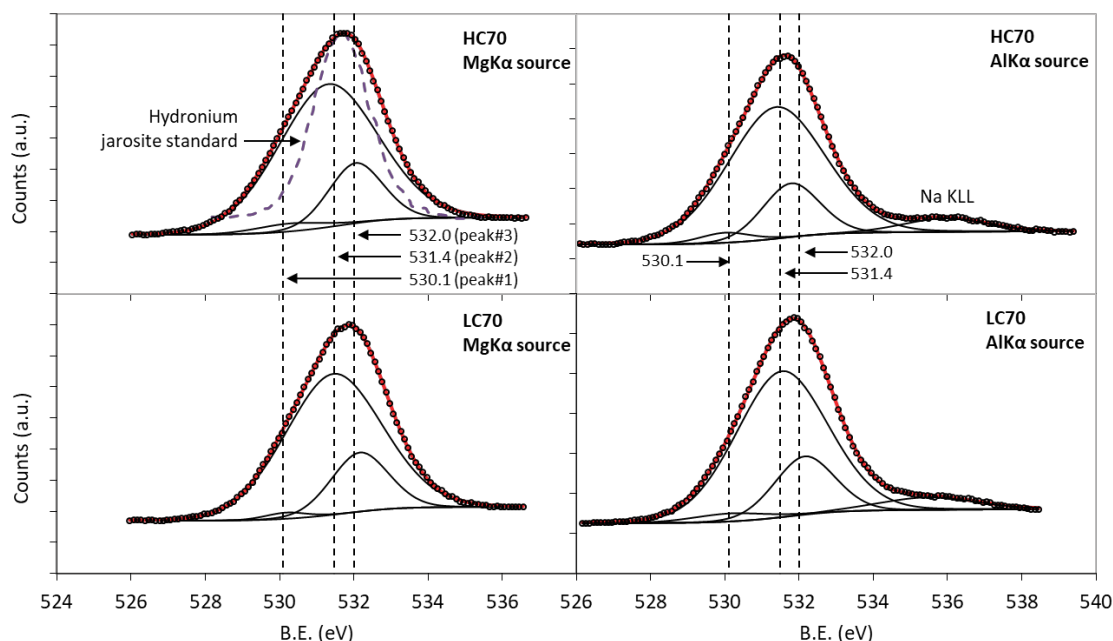


FIGURE 6. Deconvolution procedures in the O1s region for all samples (adventitious carbon as reference). The data for the hydronium jarosite standard plot were extracted from the work by Parker (2008). (Color online.)

sulfates (Sandström et al. 2002; Gard et al. 2020). The Fe2p3/2 region is formed by two peaks (Fig. 7) at ~711 and ~712 eV. These binding energy values are typically assigned to Fe(III) in jarosite-type minerals (Xu et al. 2013; Wang et al. 2021).

Finally, Table 3 shows how the binding energy values of the peaks confirming the Fe2p3/2 region are more scattered than the B.E. values for the other regions. There seems to be a dependence of the peak 1 binding energy with the amount of hydronium (w), as shown in Figure 8, which might arise from the effect of the H_3O^+ cations on the ionic distance between the Fe^{3+} cations and the SO_4^{2-} and OH^- anions.

From the B.E. assignments described above, the fittings shown in Figure 7 are the result of minimizing the sum of the curve fitting errors and the errors from the charge balance equation $2s + w + x + 3y - 2 - z = 0$, in which the different variables are the stoichiometric coefficients of the generic formulas $(FeOOH)_v(H_3O^+)_wNa_xFe_y^3SO_4^-(OH)_z$. During the deconvolution process, the coefficients are continuously re-evaluated with the values of the different peak areas. This procedure guaranteed perfect fits (Fig. 6) while keeping the electrical neutrality of the sample surface. Table 4 shows the results.

The hydronium to sulfate molar ratio (w) is always slightly lower on the most external area of the particles (MgKα source).

This is probably due to some water elimination from the external surface of the particles in the vacuum prevailing in the XPS chamber. According to the XRD results, which show that the bulk is mainly composed of natrojarosite, the w and v values must diminish to 0 toward the center of the particles, while the x , y , and z values must become 0.5, 1.5, and 3, respectively.

Kinetics

The method called “time to a given fraction” (Putnis 1992) was used to determine the transformation kinetic from Shm into NaJrs and its apparent activation energy (E_a). This method establishes that the transformed fraction (Y) and time (t) are related by an exponential function in which t is the dependent variable instead the kinetic constant (K) that is used in standard empirical kinetic models. When the reaction mechanism does not change over the temperature range studied, t_Y can be calculated by:

TABLE 4. XPS compositions: $(FeOOH)_v(H_3O^+)_wNa_xFe_y^3SO_4^-(OH)_z$

Sample	v	w	x	y	z
HC70 (Mg)	0.19	1.14	0.60	0.34	0.78
HC70 (Al)	0.22	1.30	0.64	0.42	1.21
LC70 (Mg)	0.08	1.01	0.24	0.25	0.00
LC70 (Al)	0.20	1.15	0.36	0.23	0.19

TABLE 3. Binding energy values (eV) obtained with C1s and Na1s referencing methods

Sample	C1s reference (284.6 eV)					Na1s reference (1071.7 eV)					
	O1s			S2p	Na1s	O1s			Fe2p3/2		S2p
	Peak 1	Peak 2	Peak 3			Peak 1	Peak 2	Peak 3	Peak 1	Peak 2	
HC70 (Mg)	530.3	531.3	532.0	168.9	1071.9	530.1	531.2	531.9	710.8	712.0	168.8
HC70 (Al)	530.0	531.4	531.8	168.8	1071.6	530.1	531.5	531.9	710.9	712.6	169.0
LC70 (Mg)	530.2	531.5	532.2	169.1	1071.8	530.1	531.4	532.1	710.7	712.1	169.0
LC70 (Al)	530.1	531.5	532.1	169.0	1071.7	530.1	531.5	532.1	711.0	712.0	169.0
Average	530.1	531.4	532.0	169.0	1071.7	530.1	531.4	532.0	710.9	712.2	168.9
St. dev.	0.1	0.1	0.2	0.1	0.1	0.0	0.2	0.1	0.2	0.3	0.1

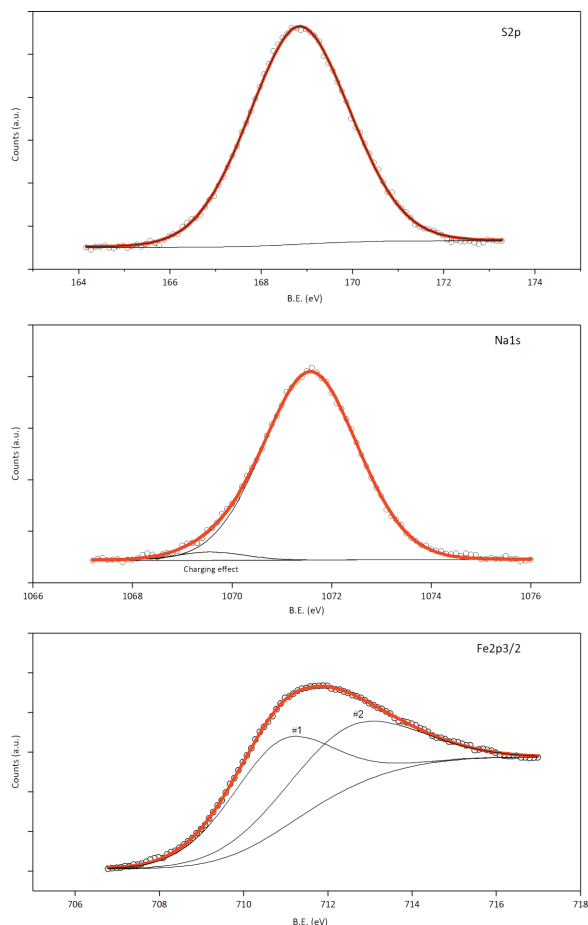


FIGURE 7. XPS results in the S2p, Na1s, and Fe2p3/2 regions for HC70 sample (AlK α source, C1s referencing method). (Color online.)

$$t_y = A^{-1} e^{\frac{E_a}{RT}} \quad (1)$$

where A is a fitting constant, R the gas constant ($8.3144 \text{ J mol}^{-1} \text{ K}^{-1}$), and T the temperature in Kelvin (K). Here, the time (t) taken to reach 95% of transformation ($t_y, y \sim 0.95$) has been estimated from a series of isothermal experiments (20, 35, 50, and 70 °C). At the beginning of the experiments, no matter what temperature is chosen, the first precipitate always corresponds to a poorly crystalline phase identified as Shm, which evolves to a crystalline phase identified as NaJrs with time. The evolution is comparable in all the series at different temperatures, but the reaction rate increases at a higher temperature. A good estimation of the transformation extent with increasing time can be checked by examining the first occurrence of the most important reflections (012, 021, and 113) of NaJrs. When these reflections are distinguished (see Fig. 3), crystals of NaJrs are predominant and the aggregates of the poorly crystalline phase have nearly disappeared. This can be considered an approximation when almost complete transformation has been accomplished. We have assumed this scenario to establish a transformation extent of about 95% ($Y \sim 95\%$). Online Materials¹ Figure S2 shows XRD diagrams obtained with increasing temperature at times when the

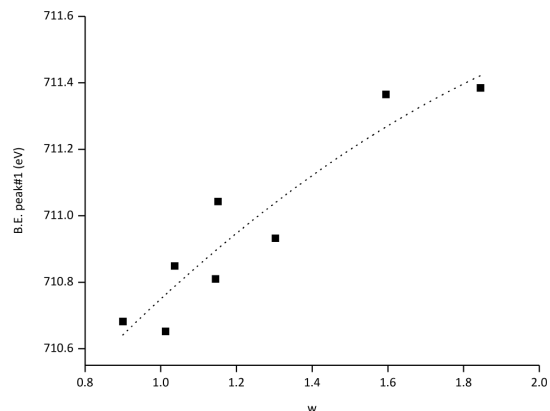


FIGURE 8. For the Fe2p3/2 region, variation of the binding energy of peak 1 with the amount of hydronium ions (w).

transformation rate is considered to be 95%. The most important reflections (012, 021, and 113) of NaJrs can be identified and the broad bands of Sch disappeared, which represented the transition to a crystalline phase. Obviously, with extended reaction times, the crystallinity degree of NaJrs increases as deduced from the decreases of FWHM values similar to that observed in Figure 3 for samples aged at 20 °C.

The experimental data of the time (t) taken to reach 95% of transformation ($t_y, y \sim 0.95$) have been plotted in Figure 9a, where $\ln t_{0.95}$ is plotted vs. $1000/T$, and the apparent activation energy has been determined from the slope of the straight line fitting these data (E_a/R). Here, a value $E_a = 52.1 \text{ kJ/mol}$, was obtained for $\sim 95\%$ of transformation from schwertmannite into natrojarosite. Previous studies have determined apparent activation energies for the NaJrs precipitation, whose values vary from 35 to 106 kJ/mol (Dutrizac 1996), which are a range of values expected given the different experimental conditions applied, such as the presence or absence of sodium jarosite seeds or the range of temperature used to calculate the activation energy.

Another suitable way to describe the progress of a trans-

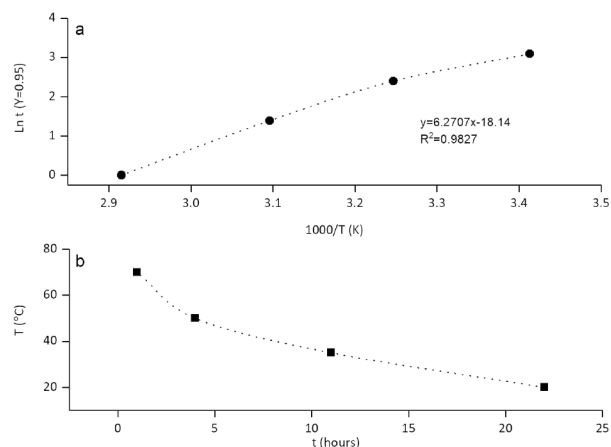


FIGURE 9. (a) Linear fitting of the time ($\ln t = 0.95$) for a 95% fraction of transformed natrojarosite vs. the reciprocal of temperature. (b) TTT graph corresponding to a fraction $Y = 0.95$ of the transformed natrojarosite.

formation is assessing experimentally a time-temperature-transformation (TTT) diagram, which indicates the time at which the transformation occurs when a sample is kept under isothermal conditions (Putnis 1992). Figure 9b displays the TTT diagram determined for the Shm to NaJrs transformation ($Y = 95$). TTT diagrams are commonly used in mineral science to deal with phase transformations (Putnis 1992; Putnis et al. 2007; Di Lorenzo et al. 2014; Jiménez and Prieto 2015). At low temperatures, the transformation begins after 1 day, and a slight increase of temperature dramatically reduces the time over which the transformation takes place. Given that the transformation rate increases with increasing temperature, the diagrams cannot be expected to have the typical “C” shape. The shape of the curve is similar to the diagrams of transformations that occur with rising temperature (Di Lorenzo et al. 2014; Jiménez and Prieto 2015).

DISCUSSION

This study underlines that knowledge of the precipitation behavior of iron oxyhydroxisulfate is one of the most important tools to understand the long-term stability of the related minerals under different geochemical environments at ambient and low-hydrothermal temperatures. The experimental results described in the previous section indicate that a poorly crystalline phase identified as schwertmannite (Fig. 2) precipitates spontaneously when ferric sulfate and sodium hydroxide solutions are mixed (Table 1) in acidic aqueous solution ($\text{pH} < 2.6$) at ambient temperature (20 °C). As aging proceeds, the aggregated nanoparticles of schwertmannite (Fig. 4a) evolve to a polycrystalline single phase, (Figs. 4b and 4c) identified as natrojarosite (Figs. 2 and 3). To understand the precipitation of Shm at ambient temperature and its rapid evolution, the initial aqueous solutions were modeled by applying the code PHREEQC (Parkhurst and Appelo 1999) to gain information on the saturation state of the liquid phase with respect to the solid phases involved at the beginning of the reaction. Thus, the saturation indexes ($\text{SI} = \text{IAP}/K$), where IAP is the ionic activity product and K is the thermodynamic solubility product, support the definition of the driving force that operates in the system. The higher the SI value, the more supersaturated the solution, and the more thermodynamically favorable the precipitation of such phase. The initial aqueous solution was highly supersaturated with respect to a significant number of solid phases: schwertmannite ($\text{SI} \sim 56.6$ and ~ 67.6), natrojarosite ($\text{SI} \sim 14.6$ and ~ 18.1), hydronium-jarosite ($\text{SI} \sim 11.8$ and ~ 14.6) and goethite ($\text{SI} \sim 8.3$ and ~ 9.9) for LC20 and HC20, respectively. Any of these phases could precipitate, but by far, the saturation indexes of schwertmannite are higher than those of jarosite-like compounds and goethite. Moreover, high SI values denote conditions far from equilibrium that can be like those prevailing in acidic mine drainages (AMD), where newly formed phases show small particle sizes and low crystallinity (Sánchez-España et al. 2012). In such extreme conditions, the low-crystallinity degree of Shm (Fig. 3) has been related to both the small size of the coherent diffraction domains and the structural disorder, which are characteristics favored by a fast precipitation process, as deduced from the morphology of the nanoparticles observed by SEM (Fig. 4a). After just one day at 20 °C (or 3 h at 70 °C), the poorly crystalline and metastable Shm transform into a crystalline phase identified as natrojarosite.

Several studies demonstrated that stable iron-bearing phases are frequently formed via metastable precursors of low-crystalline degree in natural and laboratory conditions (Waychunas et al. 1995; Bigham et al. 1996; Barham 1997; Jönsson et al. 2005; Desborough et al. 2010; Sánchez-España et al. 2012). The results here show that the transformation of Shm into NaJrs involves the decrease of the solution pH (Fig. 1), variations in the color of the precipitates (Figs. 2 and 3) and a morphological evolution from shapeless aggregates to homogeneous rhombohedral-shaped crystals (Fig. 4). These changes are the result of reactions that can be ascribed to a solvent-mediated crystallization process (Cardew and Davey 1985) in which the dissolution of the metastable phase (Shm) is concomitant with the precipitation of the stable and crystalline phase via an aqueous solution. The stable phase has been identified by XRD as Na-rich member of the $(\text{Na}, \text{H}_3\text{O})\text{Fe}_3(\text{SO}_4)(\text{OH})_6$ solid solution (Figs. 2 and 3). FTIR and XPS analyses show that part of the cationic sites on the surface of the NaJrs, in which part of the cationic sites has been replaced by hydronium ions, confirms the mineralogical composition determined by XRD. The spectroscopic analysis also suggests that a small fraction of the surface iron remains as goethite (αFeOOH). Although this phase has not been identified by XRD analysis, it could be present in proportions below the XRD detection limit. Its presence is not surprising as Shm transforms into goethite (αFeOOH) by means of gradual hydrolysis reactions accompanied by the acidification of the aqueous solution at ambient temperature (Bigham et al. 1996).

The mineral transformation mechanism can be assisted by the similarities between the crystal structure of Shm and NaJrs, such as the local octahedral coordination of Fe, which is a shared-corner with sulfate tetrahedra (Basciano and Peterson 2008; Fernandez-Martinez et al. 2010). Several reactions involve adsorption of SO_4^{2-} and H_3O^+ , which then diffuse within the crystal structure, and the parallel transport of Fe(III) from the solid to the solution, whereas OH^- and Na^+ move in the opposite direction (Figs. 5, 6, and 7), could explain the major structural rearrangement of the Shm to form NaJrs. However, the lack of a complete description of the crystal structure of Shm is a serious obstacle for the proper interpretation of the transformation in structural terms. Additionally, previous experimental studies carried out at ambient temperature demonstrated that the presence of Na destabilizes the surface of Shm, promoting its dissolution with the simultaneous precipitation of natrojarosite when a lower ferric sulfate concentration is used (Jiménez et al. 2019). Our present results confirm that Na-bearing aqueous solutions at lower temperatures (20–70 °C) favor a quick destabilization of the Shm surface under conditions far from equilibrium. After the transformation is completed, the unit-cell parameters remain stable with time while its crystallinity increases, proving that NaJrs is the only stable phase under the conditions used here (Figs. 2 and 3). The structure stability is guaranteed through the arrangement of $\text{Fe}(\text{OH})_6$ octahedra in (001) layers, which are connected by the alkali cation (Na^+) coordinated with six oxygen atoms and six OH groups forming an icosahedron. Due to these features, the structure of jarosite-like compounds is flexible enough to accommodate foreign ions. The fast transformation of schwertmannite into NaJrs under the conditions used in this work confirms that schwertmannite cannot be considered an

efficient phase for the immobilization of contaminating metals in the long term (Regenspurg and Peiffer 2005; Cruz-Hernández et al. 2016). On the contrary, natrojarosite, harboring cations and anions in its structure, remains stable in highly acid solutions for a long time, which indicates that this phase should be considered more reliable in retaining heavy metals.

A detailed spectroscopic study (Figs. 5, 6, and 7) also provides additional support for the interpretation that the crystal structure of jarosite-like minerals preserves geochemical evidence of the aqueous solutions where they were formed. The comparison of the amount of iron evaluated by XPS with different sources ($AlK\alpha$ and $MgK\alpha$, see Table 2) suggests that the iron concentration either increases or decreases toward the center of the NaJrs particles in either the LC or HC precipitates, respectively. Thus, the transformation of Shm into NaJrs seems to be a surface-controlled process clearly affected by the concentration of the precursors in the hydrothermal solution. According to Transition State Theory, the activation energy is an estimation of the energetic barrier that hinders the transformation of the metastable phase identified as schwertmannite into the thermodynamically stable natrojarosite. It is worth mentioning that acid mine drainages present similar values of sulfate concentration and pH to those of the solutions used in this work.

IMPLICATIONS

The present study focused on the formation of jarosite-like compounds that give support to previous geological, environmental, and planetary investigations because the presence of these compounds is associated with supergene deposits and acidic rock drainages and has also been verified on the surface of Mars. Mineralogical and geochemical results reveal that transformation processes between ferric-hydroxysulfates during experimentally induced reactions take place in highly ferric and sulfate concentrated aqueous solutions at temperatures between 20 and 70 °C, which reproduce the extremely acidic conditions that occur in scenarios analogous to those of acid mine drainages and epithermal ore deposits. Moreover, detailed spectroscopic studies (FTIR and XPS) suggest that both the surface and the crystal structure of jarosite-like minerals preserve geochemical evidence of the aqueous solutions where they were formed. The formation of ferric-bearing minerals during early weathering processes and hydrothermal mineral genesis plays a key role in the geochemical processes occurring in supergene exploitable deposits and hence, the presence of these minerals is of major interest for prospection and mining. The transformation of schwertmannite into natrojarosite under conditions close to those achieved in acidic mine drainages over a timescale of hours has significant environmental effects on the mobility of metals in soils and aquatic systems. The present results allow us to discard transformation mechanisms other than dissolution-precipitation, and the kinetic study indicates that the transformation of schwertmannite into natrojarosite at ambient temperature occurs over a timescale of hours. Our results reveal that schwertmannite cannot be considered an efficient phase for the immobilization of contaminating metals in the long term, whereas natrojarosite remaining stable under conditions of high acidity for long reaction times, can be considered more reliable to retain foreign ions such as heavy metals or rare earths.

AUTHOR CONTRIBUTIONS AND ACKNOWLEDGMENTS

All authors have given approval to the final version of the manuscript. The authors thank comments from two anonymous referees and assistance of the American Mineralogist editorial staff. We also thank the technical support provided by Servicios Científico-Técnicos de la Universidad de Oviedo.

FUNDING

This work was supported by the Spanish Ministry of Economy and Competitiveness project (CGL2016-77138-C2-2-P) and the University of Oviedo.

REFERENCES CITED

- Acero, P., Ayora, C., Torrentó, C., and Nieto, J.M. (2006) The behavior of trace elements during schwertmannite precipitation and subsequent transformation into goethite and jarosite. *Geochimica et Cosmochimica Acta*, 70, 4130–4139.
- Arribas, A. Jr (1995) Characteristics of high-sulfidation epithermal deposits, and their relation to magmatic fluid. *Mineralogical Association of Canada Short Course*, 23, 419–454.
- Asta, M.P., Cama, J., Martínez, M., and Giménez, J. (2009) Arsenic removal by goethite and jarosite in acidic conditions and its environmental implications. *Journal of Hazardous Materials*, 171, 965–972.
- Audi, A.A., and Sherwood, P.M.A. (2000) X-ray photoelectron spectroscopic studies of sulfates and bisulfates interpreted by $X\alpha$ and band structure calculations. *Surface and Interface Analysis*, 29, 265–275.
- Barham, R.J. (1997) Schwertmannite: A unique mineral, contains a replaceable ligand, transforms to jarosites, hematites, and/or basic iron sulfate. *Journal of Materials Research*, 12, 2751–2758.
- Basciano, L.C., and Peterson, R.C. (2007) Jarosite-hydronium jarosite solid-solution series with full iron site occupancy: mineralogy and crystal chemistry. *American Mineralogist*, 92, 1464–1473.
- (2008) Crystal chemistry of the natrojarosite-jarosite and natrojarosite-hydronium jarosite solid-solution series: A synthetic study with full Fe site occupancy. *American Mineralogist*, 93, 853–862.
- Bigham, J.M., and Nordstrom, D.K. (2000) Iron and aluminum hydroxysulfates from acid sulfate waters. *Reviews in Mineralogy and Geochemistry*, 40, 351–403.
- Bigham, J.M., Schwertmann, U., Carlson, L., and Murad, E. (1990) A poorly crystallized oxyhydroxysulfate of iron formed by bacterial oxidation of Fe(II) in acid mine waters. *Geochimica et Cosmochimica Acta*, 54, 2743–2758.
- Bigham, J.M., Carlson, L., and Murad, E. (1994) Schwertmannite, a new iron oxyhydroxysulphate from Pyhäsalmi, Finland, and other localities. *Mineralogical Magazine*, 58, 641–648.
- Bigham, J.M., Schwertmann, U., Traina, S.J., Winland, R.L., and Wolf, M. (1996) Schwertmannite and the chemical modeling of iron in acid sulfate waters. *Geochimica et Cosmochimica Acta*, 60, 2111–2121.
- Bishop, J.L., and Murad, E. (2005) The visible and infrared spectral properties of jarosite and alunite. *American Mineralogist*, 90, 1100–1107.
- Brophy, G.P., and Sheridan, M.F. (1965) Sulfate studies IV: The jarosite-natrojarosite-hydronium jarosite solid solution series. *American Mineralogist*, 50, 1595–1607.
- Burns, R.G. (1987) Ferric sulfates on Mars. *Journal of Geophysical Research: Solid Earth*, 92, E570–E574.
- Burton, E.D., Bush, R.T., Johnston, S.G., Watling, K.M., Hocking, R.K., Sullivan, L.A., and Parker, G.K. (2009) Sorption of arsenic (V) and arsenic (III) to schwertmannite. *Environmental Science & Technology*, 43, 9202–9207.
- Cardew, P., and Davey, R. (1985) The kinetics of solvent-mediated phase transformations. *Proceedings of the Royal Society of London. A. Mathematical and Physical Sciences*, 398, 415–428.
- Casas, J.M., Paipa, C., Godoy, I., and Vargas, T. (2007) Solubility of sodium-jarosite and solution speciation in the system Fe(III)-Na-H₂SO₄-H₂O at 70°C. *Journal of Geochemical Exploration*, 92, 111–119.
- Cheng, Z., Hu, Y., Wu, K., Xing, Y., Pan, P., Jiang, L., Mao, J., Ni, C., Wang, Z., Zhang, M., and others. (2020) Si/TiO₂/Ti₂O₃ composite carbon nanofiber by one-step heat treatment with highly enhanced ion/electron diffusion rates for next-generation lithium-ion batteries. *Electrochimica Acta*, 337, 135789.
- Cruz-Hernández, P., Pérez-López, R., Parviainen, A., Lindsay, M.B.J., and Nieto, J.M. (2016) Trace element-mineral associations in modern and ancient iron terraces in acid drainage environments. *CATENA*, 147, 386–393.
- Desborough, G.A., Smith, K.S., Lowers, H.A., Swayze, G.A., Hammarstrom, J.M., Diehl, S.F., Leinz, R.W., and Driscoll, R.L. (2010) Mineralogical and chemical characteristics of some natural jarosites. *Geochimica et Cosmochimica Acta*, 74, 1041–1056.
- Di Lorenzo, F., Rodríguez-Galán, R.M., and Prieto, M. (2014) Kinetics of the solvent-mediated transformation of hydromagnesite into magnesite at different temperatures. *Mineralogical Magazine*, 78, 1363–1372.
- Diao, R., Rong, J., Wang, X., Yao, Y., Zhan, Z., and Yu, X. (2018) Surface analysis and electrochemical corrosion behavior of anodic oxide films on pure titanium. *International Journal of Electrochemical Science*, 13, 7765–7777.

- Drouet, C., and Navrotsky, A. (2003) Synthesis, characterization, and thermochemistry of K-Na-H₂O jarosites. *Geochimica et Cosmochimica Acta*, 67, 2063–2076.
- Dutrizac, J. (1996) The effect of seeding on the rate of precipitation of ammonium jarosite and sodium jarosite. *Hydrometallurgy*, 42, 293–312.
- Dutrizac, J., and Kaiman, S. (1976) Synthesis and properties of jarosite-type compounds. *Canadian Mineralogist*, 14, 151–158.
- Fairén, A.G., Davila, A.F., Lim, D., Bramall, N., Bonaccorsi, R., Zavaleta, J., Uceda, E.R., Stoker, C., Wierzchos, J., Dohm, J.M., and others. (2010) Astrobiology through the ages of Mars: The study of terrestrial analogues to understand the habitability of Mars. *Astrobiology*, 10, 821–843.
- Feliu, S., Samaniego, A., El-Hadad, A.A., and Llorente, I. (2013) The effect of NaHCO₃ treatment time on the corrosion resistance of commercial magnesium alloys AZ31 and AZ61 in 0.6 M NaCl solution. *Corrosion Science*, 67, 204–216.
- Fernandez-Martínez, A., Timon, V., Roman-Ross, G., Cuello, G.J., Daniels, J.E., and Ayora, C. (2010) The structure of schwertmannite, a nanocrystalline iron oxyhydroxysulfate. *American Mineralogist*, 95, 1312–1322.
- Fernández-Pérez, A., and Marbán, G. (2020) Titanium dioxide: A heterogeneous catalyst for dark peroxidation superior to iron oxide. *Journal of Environmental Chemical Engineering*, 8, 104254.
- Gagliano, W.B., Brill, M.R., Bigham, J.M., Jones, F.S., and Traina, S.J. (2004) Chemistry and mineralogy of ochreous sediments in a constructed mine drainage wetland. *Geochimica et Cosmochimica Acta*, 68, 2119–2128.
- Gard, F.S., Santos, D.M., Daizo, M.B., Freire, E., Reinoso, M., and Halac, E.B. (2020) Pigments analysis of an Egyptian cartonnage by means of XPS and Raman spectroscopy. *Applied Physics A*, 126, 218.
- Greczynski, G., and Hultman, L. (2020) X-ray photoelectron spectroscopy: Towards reliable binding energy referencing. *Progress in Materials Science*, 107, 100591.
- Grohol, D., and Nocera, D.G. (2002) Hydrothermal oxidation–reduction methods for the preparation of pure and single crystalline alunites: Synthesis and characterization of a new series of vanadium jarosites. *Journal of the American Chemical Society*, 124, 2640–2646.
- Grosvenor, A.P., Kobe, B.A., Biesinger, M.C., and McIntyre, N.S. (2004) Investigation of multiplet splitting of Fe 2p XPS spectra and bonding in iron compounds. *Surface and Interface Analysis Surf Analysis*, 36, 1564–1574.
- Jiménez, A., and Prieto, M. (2015) Thermal stability of ettringite exposed to atmosphere: Implications for the uptake of harmful ions by cement. *Environmental Science & Technology*, 49, 7957–7964.
- Jiménez, A., Hernández, A., and Prieto, M. (2019) Crystallization behaviour of iron-hydroxide sulphates by aging under ambient temperature conditions. *Minerals*, 9, 27.
- Jin, X., Li, X., Guo, C., Jiang, M., Yao, Q., Lu, G., and Dang, Z. (2020) Fate of oxalic-acid-intervened arsenic during Fe(II)-induced transformation of As(V)-bearing jarosite. *The Science of the Total Environment*, 719, 137311.
- Jönsson, J., Persson, P., Sjöberg, S., and Lövgren, L. (2005) Schwertmannite precipitated from acid mine drainage: phase transformation, sulphate release and surface properties. *Applied Geochemistry*, 20, 179–191.
- Khalid, M.K., Leiviskä, T., and Tanskanen, J. (2017) Properties of vanadium-loaded iron sorbent after alkali regeneration. *Water Science and Technology: A Journal of the International Association on Water Pollution Research*, 76, 2672–2679.
- Langford, J.I., and Wilson, A. (1978) Scherrer after sixty years: a survey and some new results in the determination of crystallite size. *Journal of Applied Crystallography*, 11, 102–113.
- Liu, A., Liu, J., Pan, B., and Zhang, W.X. (2014) Formation of lepidocrocite (γ -FeOOH) from oxidation of nanoscale zero-valent iron (nZVI) in oxygenated water. *RSC Advances*, 2014, 4, 57377–57382.
- Madden, M.E., Bodnar, R., and Rimstidt, J. (2004) Jarosite as an indicator of water-limited chemical weathering on Mars. *Nature*, 431, 821–823.
- Majzlan, J., Alpers, C.N., Koch, C.B., McCleskey, R.B., Myneni, S.C.B., and Neil, J.M. (2011) Vibrational, X-ray absorption, and Mössbauer spectra of sulfate minerals from the weathered massive sulfide deposit at Iron Mountain, California. *Chemical Geology*, 284, 296–305.
- Nordstrom, D.K. (2009) Acid rock drainage and climate change. *Journal of Geochimical Exploration*, 100, 97–104.
- Parker, A.D. (2008) Oxidative dissolution of chalcopyrite in ferric Media: An X-ray photoelectron spectroscopy study. Curtin University of Technology. School of Science and Computing.
- Parkhurst, D.L., and Appelo, C.A.J. (1999) User's guide to PHREEQC (ver. 2): A computer program for speciation, batch-reaction, one-dimensional transport, and inverse geochemical calculations. Water-Resources Investigations Report 99-4259. <https://doi.org/10.3133/wri994259>
- Powers, D.A., Rossman, G.R., Schugar, H.J., and Gray, H.B. (1975) Magnetic behavior and infrared spectra of jarosite, basic iron sulfate, and their chromate analogs. *Journal of Solid State Chemistry*, 13, 1–13.
- Prasad, P.S.R., Shiva Prasad, K., Krishna Chaitanya, V., Babu, E.V.S.S.K., Sreedhar, B., and Ramana Murthy, S. (2006) In situ FTIR study on the dehydration of natural goethite. *Journal of Asian Earth Sciences*, 27, 503–511.
- Putnis, A. (1992) An Introduction to Mineral Sciences. Cambridge University Press.
- Putnis, C.V., Geisler, T., Schmid-Beurmann, P., Stephan, T., and Giampaolo, C. (2007) An experimental study of the replacement of leucite by analcime. *American Mineralogist*, 92, 19–26.
- Regenspurg, S., and Peiffer, S. (2005) Arsenate and chromate incorporation in schwertmannite. *Applied Geochemistry*, 20, 1226–1239.
- Sánchez-España, J., Pamo, E.L., Pastor, E.S., Andrés, J.R., and Rubí, J.A.M. (2006) The removal of dissolved metals by hydroxysulphate precipitates during oxidation and neutralization of acid mine waters, Iberian Pyrite Belt. *Aquatic Geochemistry*, 12, 269–298.
- Sánchez-España, J., Yusta, I., and López, G.A. (2012) Schwertmannite to jarosite conversion in the water column of an acidic mine pit lake. *Mineralogical Magazine*, 76, 2659–2682.
- Sandström, M., Jalilehvand, F., Persson, I., Gelius, U., Frank, P., and Hall-Roth, I. (2002) Deterioration of the seventeenth-century warship *Vasa* by internal formation of sulphuric acid. *Nature*, 415, 893–897.
- Sangwal, K. (1999) Kinetic effects of impurities on the growth of single crystals from solutions. *Journal of Crystal Growth*, 203, 197–212.
- Schwertmann, U., Bigham, J.M., and Murad, E. (1995) The first occurrence of schwertmannite in a natural stream environment. *European Journal of Mineralogy*, 7, 547–552.
- Sotiropoulou, S., Perdikatsis, V., Birtacha, K., Apostolaki, C., and Devetzi, A. (2012) Physicochemical characterization and provenance of colouring materials from Akrotiri-Thera in relation to their archaeological context and application. *Archaeological and Anthropological Sciences*, 4, 263–275.
- Wang, X., Xie, Y., Tong, W., Hu, W., Wang, Y., and Zhang, Y. (2021) Photochemical degradation of chloramphenicol over jarosite/oxalate system: Performance and mechanism investigation. *Journal of Environmental Chemical Engineering*, 9, 104570.
- Waychunas, G.A., Xu, N., Fuller, C.C., Davis, J.A., and Bigham, J.M. (1995) XAS study of AsO₄³⁻ and SeO₄²⁻ substituted schwertmannites. *Physica B: Condensed Matter*, 208-209, 481–483.
- Xu, Z., Liang, J., and Zhou, L. (2013) Photo-Fenton-like degradation of azo dye methyl orange using synthetic ammonium and hydronium jarosite. *Journal of Alloys and Compounds*, 546, 112–118.
- Yu, J.Y., Heo, B., Choi, I.K., Cho, J.P., and Chang, H.W. (1999) Apparent solubilities of schwertmannite and ferrihydrite in natural stream waters polluted by mine drainage. *Geochimica et Cosmochimica Acta*, 63, 3407–3416.

MANUSCRIPT RECEIVED SEPTEMBER 6, 2021

MANUSCRIPT ACCEPTED JANUARY 19, 2022

ACCEPTED MANUSCRIPT ONLINE JANUARY 26, 2022

MANUSCRIPT HANDLED BY DI WU

Endnote:

¹Deposit item AM-23-18288, Online Materials. Deposit items are free to all readers and found on the MSA website, via the specific issue's Table of Contents (go to http://www.minsocam.org/MSA/AmMin/TOC/2023/Jan2023_data/Jan2023_data.html).